


Article

Micro-Groove Optimisation of High-Speed Inner Ring Micro-Grooved Pumping Seal for New Energy Electric Vehicles

Hanqing Chen ^{1,2,*}, Ruqi Yan ³ , Xianzhi Hong ⁴, Xin Bao ⁴ and Xuexing Ding ^{1,*}¹ School of Petrochemical Engineering, Lanzhou University of Technology, Lanzhou 730050, China² School of Mechanical Engineering, Lanzhou Petrochemical University of Vocational Technology, Lanzhou 730060, China³ School of Chemistry and Chemical Engineering, Lanzhou Jiaotong University, Lanzhou 730070, China; yanruqima@126.com⁴ Chengdu Yitong Seal Co., Ltd., Chengdu 610100, China; hongxianzhi@cdytseal.com (X.H.); baoxin@cdytseal.com (X.B.)

* Correspondence: 181080706002@lut.edu.cn (H.C.); dingxxseal@126.com (X.D.); Tel.: +86-188-9348-6963 (X.D.)

Abstract: Traditional oil seals are insufficient for the high-speed and bi-directional rotation of new energy electric vehicles. Therefore, we developed a Python program focusing on micro-groove pump seals and examined the unexplored non-contact oil–air biphasic internal end-face seals. Real gas effects were described using the virial and Lucas equations. We introduced an oil–air ratio to determine the equivalent density and viscosity of the two-phase fluid in the seal. Furthermore, we solved the compressible steady-state Reynolds equation using the finite difference method. Analysing the seal’s pumping mechanisms and the effects of operating parameters on sealing performance, we assessed 17 types of hydrodynamic grooves. The results demonstrate that inverse fir tree-like grooves perform well under typical sealing conditions. Under the conditions given in this study, the pumping rate of the optimal groove type compared to other groove types even reached 633.54%. In the oil–air biphasic state, the micro-groove pump seal exerts significant dynamic pressure on the sealing surface. Seal opening force increases with rotational velocity, oil–air ratio, and inlet pressure but decreases with temperature. The pumping rate first increases and then decreases with rotational velocity, increases with oil–air ratio and temperature, and then decreases with inlet pressure. Some special working points require consideration in sealing design. Our results provide insights into designing micro-grooved pumping seals for new energy electric vehicles.

Keywords: new energy electric vehicle; micro-grooved pumping seal; real gas effect; oil–air two-phase flow; micro-groove optimisation; sealing performance



Citation: Chen, H.; Yan, R.; Hong, X.; Bao, X.; Ding, X. Micro-Groove Optimisation of High-Speed Inner Ring Micro-Grooved Pumping Seal for New Energy Electric Vehicles. *Processes* **2024**, *12*, 1281. <https://doi.org/10.3390/pr12061281>

Academic Editor: Takuya Oda

Received: 17 May 2024

Revised: 15 June 2024

Accepted: 19 June 2024

Published: 20 June 2024



Copyright: © 2024 by the authors. Licensee MDPI, Basel, Switzerland. This article is an open access article distributed under the terms and conditions of the Creative Commons Attribution (CC BY) license (<https://creativecommons.org/licenses/by/4.0/>).

1. Introduction

New energy electric vehicle (EV) drivetrains feature high efficiency and integration, lightweight, and low noise and vibrations [1,2]. Moreover, the performance of EVs is closely related to the electric drivetrain system [3,4], which provides high reliability, high power density, wide speed regulation range, and strong overload capacity. The high-speed performance of the oil seal is currently a technical limitation, constraining the development of electric drivetrain systems [5]. The oil seal is a precision part and critical component of an electric motor. High-reliability motors require high-performance bearings, and high-reliability long-service-life bearings must be guaranteed by oil seals.

The working conditions of traditional fuel vehicle engines and EV power systems are similar. Therefore, rubber skeleton [6,7] and polytetrafluoroethylene (PTFE) [8–10] oil seals have been widely employed in electric drivetrain systems. Rubber skeleton seals have a maximum allowable linear speed of approximately 38 m/s but perform poorly under reverse rotation. While rubber skeleton oil seals with bi-directional backflow grooves have been developed [11], their backflow performance is inferior to that of unidirectional

backflow grooves [12]. Additionally, the maximum allowable linear speed of oil seals with bi-directional backflow grooves is 30 m/s. Although PTFE oil seals with spiral grooves have a maximum allowable linear speed of 60 m/s [13,14], they perform poorly under reverse rotation because of the unidirectional pumping characteristic of spiral grooves. Existing oil seals have a less-than-desirable performance under a linear speed exceeding 40 m/s or in bi-directional working conditions. Seal failure not only significantly reduces the performance of electric drive systems but also leads to environmental pollution caused by lubricant oil leakage. Therefore, we proposed a pumping seal with micro-grooves for high-speed electric drivetrains. The proposed seal is a non-contact hydrodynamic seal whose performance is unaffected by high-speed rotations. Laser-engraved hydrodynamic grooves are designed to rotate in two directions, enabling the seal to function properly under reverse rotation of the electric motor. In particular, several researchers have studied bi-directional rotating hydrodynamic grooves [15–23] involving various groove types. However, most of these studies have only focused on one or two types of grooves. Thus, determining which groove type has the greatest advantage in bi-directional rotation is challenging. Almost all the hydrodynamic grooves for upstream pumping seals in the literature were located near the outer edge of the carbon ring face, close to the high-pressure area. This study applied a unique high-speed micro-groove pumping seal for EVs by opening the hydrodynamic grooves near the inner edge of the carbon ring face close to the low-pressure area.

The micro-grooved pumping seal operates at high speeds and involves gas and liquid phases; thus, this seal can be categorised as an oil–air two-phase seal. In recent years, oil–air two-phase lubrication sealing technology has been widely used in high-speed rotating machines owing to its high efficiency, good lubrication performance, and low energy consumption. Polling et al. [24] generalised equations for computing various properties of finite volumes of gases and liquids using extensive experimental data. Li et al. [25–27] investigated the dynamic characteristics of oil–air two-phase dynamic seals and the effects of thermal load, mechanical load, and constraints on the microdeformation of the dynamic ring end face by establishing the steady- and dynamic-state Reynolds equations of the oil–air two-phase flow and an analytical model considering thermal–solid coupling. Li et al. [28–32] analysed the effects of operating and end-face-structure parameters on the gas- and liquid-phase performance parameters of dynamic seals and proposed an equation for computing equivalent viscosity by establishing a numerical analysis model of the gas and liquid phases in the flow domain near the end face of dynamic seals. Chen et al. [33] investigated the end-face temperature distribution of a two-phase backflow seal in open and non-open states. Li et al. [34,35] established a model of the fluid between the end faces of a two-phase seal to obtain the thermal and mechanical deformations of the end faces and the pressure, velocity, and phase distribution in the flow field between the end faces. While the above studies provide references for the research on oil–gas two-phase micro-groove pumping seals, they are mostly based on fixed physical parameters.

In response to the complex operating conditions of micro-groove pumping seals for new energy vehicles, which operate at high speeds and deal with gas–liquid two-phase flows, this study aims to obtain the optimal fluid pumping dynamic pressure groove structure and investigate the variation patterns of its sealing performance. We focus on micro-groove pumping seals, employing the compressible steady-state Reynolds equation and utilising the Virial equation and the Lucas equation to describe the actual gas effects and viscosity changes. We introduce the oil–air ratio to determine the equivalent density and viscosity. Through numerical calculations, we analyse the pumping mechanism of micro-groove pumping seals. Subsequently, we conduct comparative analyses of various groove structures to select the optimal dynamic pressure groove type. Furthermore, under the optimal groove-type structure, we analyse and discuss the relationship between operating parameters (rotational velocity, oil–air ratio, inlet pressure, and temperature) and steady-state sealing performance. This study provides theoretical support for the design of micro-groove pumping seals for future new energy vehicles and actively promotes advancements in new energy electric vehicles and sealing technology.

2. Theoretical Model

2.1. Geometric Model

Figure 1 shows the structure of the proposed micro-grooved pumping seal for EVs. The rotating and stationary rings are mounted in the seal chamber. The shaft liner, designed with a seat to hold the rotating ring, is connected to the shaft using an anti-rotation pin. The shaft liner connection is sealed using an O-ring. The anti-rotation pin fixes the rotating ring and shaft in both the rotational and axial directions (preventing the rotation ring from rotating around and moving along the axis of the shaft). The stationary ring is mounted in a seat and is connected to the cover of the seal using a bellow (wave spring). The bellow is highly flexible and can compensate for random variations. It functions as both an elastic element and a seal. The cover and chamber of the seal are connected with bolts, and the connection is sealed with a washer. The bellow, rotating, and stationary rings are compressed against each other. During the operating state of the micro-grooved pumping seal, oil–air lubricant flows from the low-pressure side (bellow side) and is pumped to the high-pressure side via the hydrodynamic grooves, forming an extremely thin oil–air two-phase film at the end face that prevents lubricant leakage. When the shaft stops rotating, the sealing face is closed, effectively preventing lubricant leakage. This structure enables the use of the oil seal for the input shaft of high-speed electric drivetrains. The seal exhibits improved strength, wear resistance, sealing performance, and reliability under the demanding operating conditions of the input shaft, significantly improving the service life and stability of the electric motor.

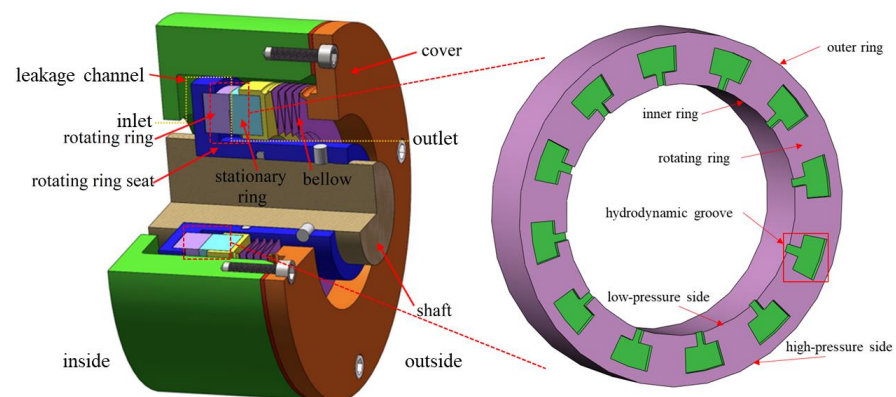


Figure 1. Schematic of the proposed micro-grooved pumping seal for EVs.

2.2. Mathematical Model

2.2.1. Pressure Control Equation

The fluid in the seal was assumed to be a Newtonian fluid, the pressure gradient in the film thickness direction is zero, the seal end surface deformation is negligible, and there is no consideration for temperature changes within the flow field. Thus, the steady-state Reynolds equation of the laminar flow field in the micro-grooved pumping seal can be expressed as [36,37]

$$\frac{1}{r} \cdot \frac{\partial}{\partial \theta} \left(\frac{\rho_e \cdot h^3}{\eta_e} \cdot \frac{\partial p}{\partial \theta} \right) + \frac{\partial}{\partial r} \left(\frac{r \cdot \rho_e \cdot h^3}{\eta_e} \cdot \frac{\partial p}{\partial r} \right) = 6 \cdot r \cdot \omega \cdot \frac{\partial}{\partial \theta} (\rho_e \cdot h) \quad (1)$$

where r is the radius of any point at the oil–air two-phase film at the end face (m), θ is the spread angle (rad), ω is the angular velocity (rad/s), h is the film thickness (m), ρ_e is the equivalent density (kg/m^3), and η_e is the equivalent viscosity ($\text{Pa}\cdot\text{s}$).

2.2.2. Equivalent Density

At high speeds, the internal lubricating oil of the electric drivetrain forms small liquid droplets, known as oil mist, due to the high-speed mechanical agitation of the rotor. This oil

mist mixes with air to form a two-phase oil–gas mixture. Therefore, to accurately describe the fluid density of the oil–gas two-phase flow passing through the seal clearance, this paper adopts equivalent density for calculation, which can be expressed as follows:

$$\rho_e = \rho_{\text{gas}} \cdot (1 - c) + \rho_{\text{oil}} \cdot c \quad (2)$$

where ρ_{gas} is the density of air (kg/m^3), ρ_{oil} is the density of the lubricant (kg/m^3), and c is the oil–air ratio (the volume fraction of oil droplets in the mixed gas).

To consider the real effect of air in the flow field on sealing performance, the air density was described using the three-term truncated virial equation as follows [24]:

$$\rho_{\text{gas}} = \frac{p}{Z \cdot R_g \cdot T} \quad (3a)$$

$$Z = \frac{p}{\rho_{\text{gas}} \cdot R_g \cdot T} \approx 1 + B \cdot \left(\frac{p}{R_g \cdot T} \right) + (C - B^2) \cdot \left(\frac{p}{R_g \cdot T} \right)^2 \quad (3b)$$

$$B \cdot \left(\frac{p_c}{R_g \cdot T_c} \right) = 0.1445 - \frac{0.330}{T_r} - \frac{0.1385}{T_r^2} - \frac{0.0121}{T_r^3} - \frac{0.000607}{T_r^8} + \varepsilon_g \cdot \left(0.0637 + \frac{0.331}{T_r^2} - \frac{0.423}{T_r^3} - \frac{0.008}{T_r^8} \right) \quad (3c)$$

$$C \cdot \left(\frac{p_c}{R_g \cdot T_c} \right)^2 = \left(0.01407 + \frac{0.02432}{T_r^{2.8}} - \frac{0.00313}{T_r^{10.5}} \right) \cdot T_r + \varepsilon_g \cdot \left(-0.02676 + \frac{0.0177}{T_r^{2.8}} + \frac{0.04}{T_r^3} - \frac{0.003}{T_r^6} - \frac{0.00228}{T_r^{10.5}} \right) \cdot T_r \quad (3d)$$

where Z is the compressibility factor, P_c is the critical pressure of air (3.786×10^6 Pa), T_c is the critical temperature of air (132.53 K), T_r is the reference state temperature ($T_r = T/T_c$), ε_g is the eccentric factor of air, and R_g is the gas constant. $R_g = R/M$, where R is the molar mass of air (28.965 kg/kmol), and M is the universal gas constant (8314 J/(kmol·K)).

2.2.3. Equivalent Viscosity

The equivalent viscosity of the two-phase fluid in the seal is computed as follows:

$$\eta_e = \eta_{\text{gas}} \cdot (1 - c) + \eta_{\text{oil}} \cdot c \quad (4)$$

where η_{gas} and η_{oil} are the air and lubricant viscosities (Pa·s), respectively.

Air viscosity is computed using the Lucas equation as follows [24]:

$$\xi = 0.176 \left(\frac{T_c}{M^3 \cdot p_c^4} \right)^{1/6} \quad (5a)$$

$$Z_1 = \eta_0 \cdot \xi = \left[0.807 T_r^{0.618} - 0.375 \exp(-0.499 T_r) + 0.304 \exp(-4.058 T_r) + 0.018 \right] \cdot F_P^O \cdot F_Q^O \quad (5b)$$

if $T_r \leq 1$, $p_r < p_{vp}/p_c$, then,

$$Z_2 = 0.600 + 0.760 p_r^\alpha + (6.990 p_r^\beta - 0.6) \cdot (1 - T_r) \quad (5c)$$

if $1 < T_r < 40$, $0 < p_r \leq 100$, then,

$$Z_2 = \eta_0 \cdot \xi \cdot \left[1 + \frac{a \cdot p_r^e}{b \cdot p_r^f + (1 + c \cdot p_r^d)^{-1}} \right] \quad (5d)$$

$$\eta_{\text{gas}} = \frac{Z_2 \cdot F_P \cdot F_Q}{\xi} \quad (5e)$$

where η_0 is the viscosity at low pressure at the same temperature; P_r is the reference-state pressure ($P_r = P/P_c$); and F_P^O , F_Q^O , F_P , F_Q , α , β , a , b , c , d , e , and f are as defined in [24].

A gear oil GL-4 (Shell Spirax S2 G 80W-90; Shell, The Hague, The Netherlands) was used as the lubricant. The effect of pressure on viscosity was negligible because the

lubricant operated at low pressures. Therefore, only the effect of temperature on viscosity was considered [37].

$$\eta_{\text{oil}} = \eta_{s0} \cdot e^{-\beta_s \cdot (T - T_{s0})} \quad (6)$$

where η_{s0} is the viscosity when the temperature is equal to T_{s0} (Pa·s), and β_s is the viscosity–temperature coefficient, which is approximately $0.0365/^\circ\text{C}$.

2.3. Boundary Conditions

One end face was defined as the inlet and the other as the outlet. The pressure at the boundary was maintained constant as follows:

$$\begin{cases} p(r = r_i) = p_o \\ p(r = r_o) = p_i \end{cases} \quad (7)$$

where P_i and P_o are the inlet and outlet pressures (MPa), respectively, and r_i and r_o are the inner and outer radii (mm) of the seal ring, respectively.

Micro-grooves are arranged periodically in the circumferential direction to establish a periodic pressure boundary within the computational domain is defined as follows:

$$p(r, \theta = \frac{\pi}{N_g}) = p(r, \theta = \frac{-\pi}{N_g}) \quad (8)$$

where N_g is the number of grooves.

2.4. Steady-State Performance Parameters

By solving the aforementioned equations and boundary conditions, the pressure distribution in the oil–air two-phase film between the seal end surface can be obtained, based on which the opening force (F_o) and leakage rate (Q_m) can be obtained as follows:

$$F_o = \int_0^{2\pi} \int_{r_i}^{r_o} p \cdot r \cdot dr d\theta \quad (9)$$

and the leakage mass rate

$$Q_m = \int_0^{2\pi} \int_0^h \rho_e \cdot u_r \cdot r \cdot dz d\theta \quad (10)$$

3. Results and Discussion

A rapid computational program was developed for simulating the flow field of micro-groove pumps. This Python program uses a visual interactive interface for inputting geometric and operational parameters. Considering actual gas effects and the equivalent density and viscosity of the oil–air two-phase flow, the program employs finite difference methods to numerically solve the pressure control equations. Finally, the results are displayed using a graphical interface. The program efficiently, accurately, and intuitively simulates the flow field, providing significant assistance in analysing the pumping mechanism and sealing characteristics.

Figure 2 shows the groove geometry; a rectangular configuration is shown for illustrative purposes. The geometry and operating parameters of the seal used for the computation are presented in Tables 1 and 2, respectively. Figure 3 shows a flowchart of the solution process.

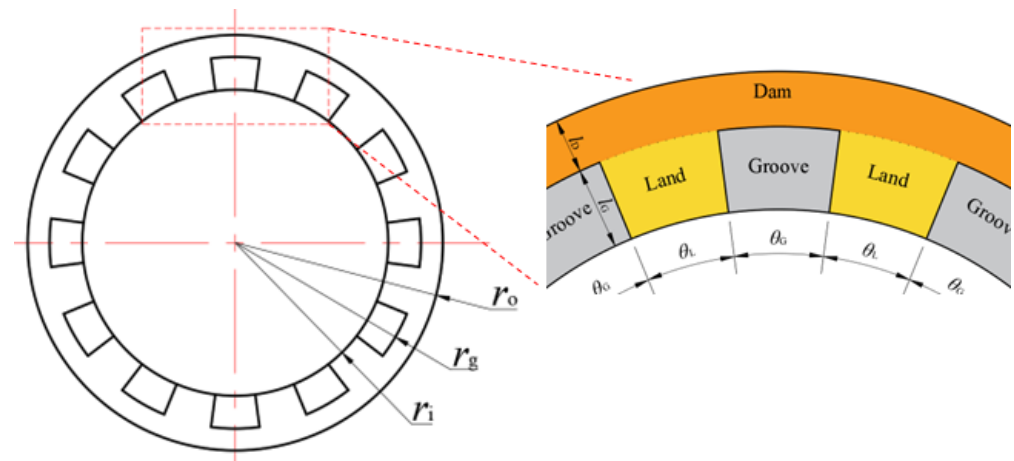


Figure 2. Schematic of the rotating ring dimensions.

Figure 1 illustrates the geometric structure of the groove-end face of the micro-groove pumping seal. The inner diameter of the sealing ring is denoted by r_i , the outer diameter by r_o , and the root diameter of the hydrodynamic groove, which is the maximum radius where the groove root is located, is denoted by r_g . The expansion angle of the groove area on the sealing face is denoted by θ_G , the expansion angle of the land area by θ_L , the equal width of the groove area and land area by l_G , and the width of the dam area by l_D . The groove–land ratio is represented by λ_{G-L} , and the groove–dam ratio is λ_{G-D} . The specific expressions are as follows:

$$\lambda_{G-L} = \theta_G / \theta_L \quad (11a)$$

$$\lambda_{G-D} = l_G / l_D = \frac{r_g - r_i}{r_o - r_g} \quad (11b)$$

$$\theta_G = \frac{\pi}{N_g} \cdot \frac{\lambda_{G-L}}{\lambda_{G-L} + 100\%} \quad (11c)$$

$$r_g = r_i + (r_o - r_i) \cdot \frac{\lambda_{G-D}}{\lambda_{G-D} + 100\%} \quad (11d)$$

Table 1. Geometric parameters of the high-speed micro-grooved pumping seal for EVs.

Parameter	Value
Outer radius r_o (mm)	38
Inner radius r_i (mm)	28
Number of grooves N_g	12
Groove depth h_g (μm)	5
Groove–land ratio λ_{G-L}	1
Groove–dam ratio λ_{G-D}	1.5
Average film thickness (end-face clearance) h_0 (μm)	4

Table 2. Operating parameters of the high-speed micro-grooved pumping seal for EVs.

Parameter	Value
Rotational velocity n (rpm)	2000–80,000
Inlet pressure p_i (kPa)	0–300
Outlet pressure p_o (kPa)	0
Temperature T ($^{\circ}\text{C}$)	60–110
Oil–air ratio c	0.01–0.1

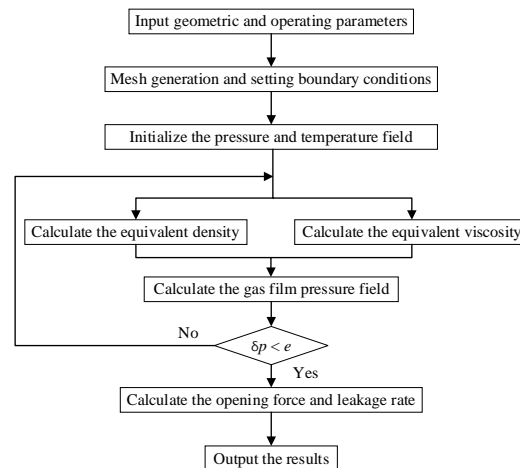


Figure 3. Flowchart of the numerical computation.

3.1. Verification

3.1.1. Grid Independence Verification

The grid size of the computational domain model of the micro-groove pumping seal was determined by considering node grids of different densities. Calculations were performed using the parameters in Tables 1 and 2, with an inlet pressure $p_i = 0.1$ MPa, inlet temperature $T_i = 100$ °C, rotational speed $n = 20,000$ r/min, and a sealing medium of two-phase flow with an oil–air ratio of 3%. The effect of the number of grids on the opening force and leakage rate is shown in Figure 4. Note that with an increase in grid density, both the opening force and leakage rate initially increase and then stabilise. The opening force and leakage rate changes are minimal when the grid density exceeds 7500. Increasing the number of grids would inevitably lead to an exponential increase in the iterative process time. Therefore, to achieve computational efficiency and result accuracy, a grid number of 11,532 was chosen in this study.

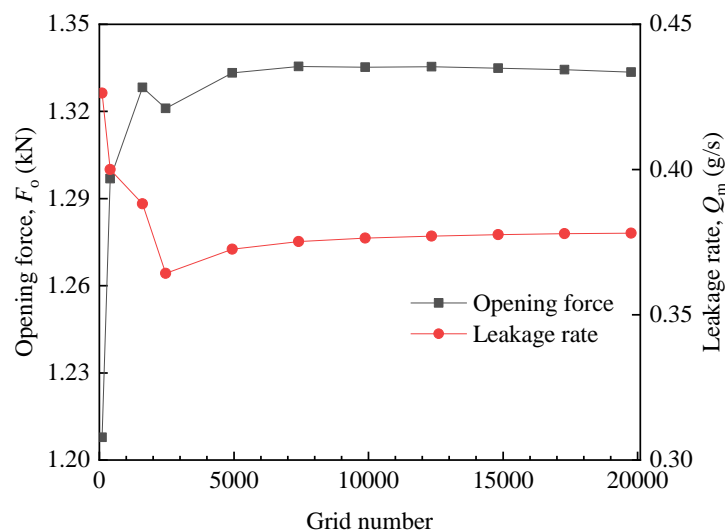


Figure 4. Grid number on the opening force and leakage rate.

3.1.2. Verification of Procedure

The lubrication equation established in [27] simultaneously considers various factors, such as the equivalent viscosity, equivalent density, and isothermal process, of oil–air two-phase fluids. This equation approaches the lubrication conditions considered in this study. Therefore, the geometric and operating parameters used in [27] (Tables 1 and 2)

were used to verify the accuracy of the aforementioned computation method, as shown in Figure 5. The computational results obtained using the proposed method are close to those obtained using the method proposed [27], with a relative error of <6%. This error is because the real gas effect and viscosity were considered in this study, and the effect of temperature on the equivalent viscosity and density of the oil–air mixture was also considered. Thus, our analysis is closer to real-world engineering scenarios.

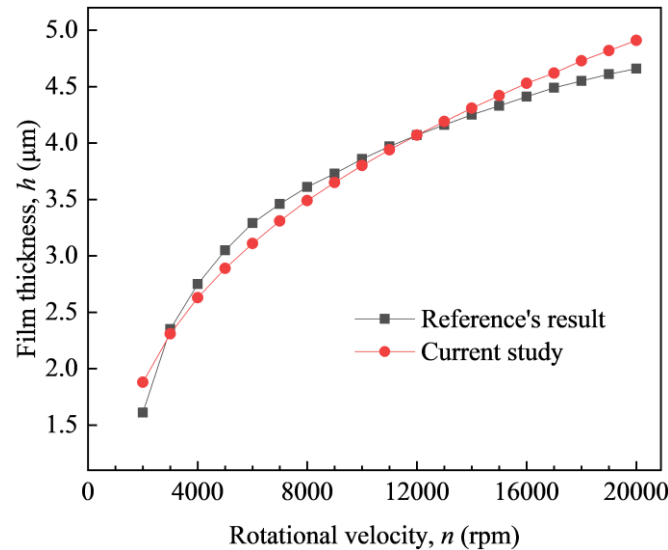


Figure 5. Verification of the computational procedure [27].

3.2. Analysis of the Flow Field in the Micro-Grooved Pumping Seal and Groove Structure Optimisation

3.2.1. Classification of Standard Bi-Directional Rotating Hydrodynamic Grooves

Table 3 presents several structural types commonly mentioned in the literature. The table expands upon them. These structures with strong symmetry are suitable for bi-directional rotation. Based on the position of the high-pressure convergence area during rotation, they can be roughly divided into four categories.

Table 3. Classification of typical bi-directional rotating hydrodynamic grooves.

Category	Groove Type
First: Straight Edge	Rectangular
	T-shaped
	Inverted T-shaped
Second: Circular Arc	Circular
	Semicircular
	Semicircular ring
	Circular arc
Third: Sharp Angle	V-shaped
	Inverted fir tree-shaped, multiple inverted fir tree-shaped
	Spindle-shaped, multiple spindle-shaped
Combined: Straight Edge with Sharp Angle	Fir tree-shaped, multiple fir tree-shaped
Combined: Circular Arc with Sharp Angle	Edge-opened Reuleaux triangular
	Angle-opened Reuleaux triangular

The first category, straight edge type, includes rectangular, T-shaped, and inverted T-shaped grooves. The boundaries of these grooves either align with the circumferential direction or with the radial direction. As the circumferential edge aligns with the direction of rotation, no fluid is accumulated to form an evident high-pressure convergence area. The area of high-pressure gas film convergence is located on the straight edge aligned with the radial direction.

The second category, circular arc type, includes circular, semicircular, and semicircular ring grooves. The high pressure in these grooves converges on the arc edge of the groove.

The third category, sharp angle type, includes fir tree-shaped, inverted fir tree-shaped, and spindle-shaped grooves. These grooves have oblique edges that do not overlap with the radial direction, guiding the flow of fluid along the oblique edge, ultimately converging with other fluids flowing along the oblique edge or the circumferential edge, forming one or more sharp-point high-pressure areas.

The fourth category, combined type, includes edge-opened Lello triangular, angle-opened Lello triangular, and variant T-shaped grooves. This category combines two of the previous three categories, forming new high-pressure boundary structure characteristics.

3.2.2. Pressure Field Distribution

To investigate the pumping mechanism of the micro-grooved pumping seal and facilitate the selection of the groove structure, the pressure distribution in a computational unit of the seal was computed using the following parameter settings: the geometric parameters of T-shaped grooves, as presented in Table 1; rotational velocity: 20,000 r/min; pressure at high-pressure side: 100 kPa; temperature: 100 °C; and oil–air ratio: 0.03. First, the pressure distribution of the T-shaped groove micro-groove pumping seal was computed for both full cycle and single cycle under 2D and 3D effects. The pressure distribution of the T-shaped groove micro-groove pumping seal, as calculated, is shown in Figure 6.

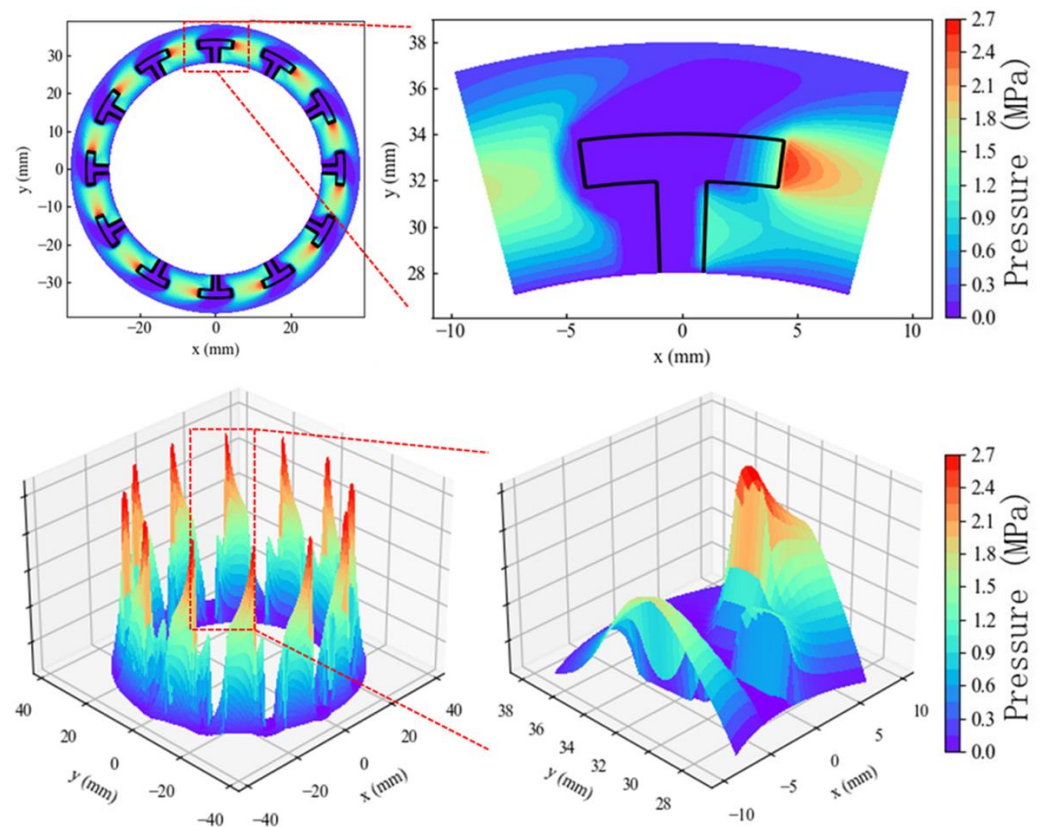


Figure 6. Pressure distribution in the micro-grooved pumping seal.

As shown in Figure 6, based on the given inlet and outlet pressures, the pressure varies nonlinearly from the low- to the high-pressure side of the flow field. When the seal ring rotates, the right side of the T-shaped groove is compressed, producing a hydrodynamic effect. Subsequently, the end-face pressure increases significantly. By contrast, on the left side of the T-shaped groove, the oil–air fluid flows into the groove from the left side as the seal ring rotates, increasing the cross-sectional area of the flow (the gap expands). No hydrodynamic effect is produced at the left boundary of the groove, and the pressure therein does not increase. The pressure distribution in the micro-grooved pumping seal exhibits periodic variations, as shown in Figure 6. A high-pressure zone is formed between the right boundary of a groove and the left boundary of the next groove. This zone functions as a pressure barrier that effectively blocks the oil–air fluid from leaking from the high- to the low-pressure side. Additionally, the grooves produced a pumping effect, thereby pumping the oil–air fluid from the low- to the high-pressure side. However, no pressure barrier was formed between the left and right sides of the same groove and between the inner and outer radius of the seal ring. Although lubricant may leak through these areas, if the pumping rate resulting from the pumping effect is larger than or equal to the leakage rate through these areas, the seal will experience no leakage. For a more straightforward comparison of the pressure distribution for each groove type, only the pressure distribution for a single cycle under 2D effects is displayed for all groove types.

Figure 7 includes the pressure distribution of typical bi-directional rotating hydrodynamic grooves belonging to the first category ((1) rectangular groove, (2) T-shaped groove, and (3) inverted T-shaped groove); the second category ((4) circular groove, (5) semicircular groove, and (6) semicircular ring groove); the third category ((7) inverted fir tree-shaped groove with one layer of branches, (8) inverted fir tree-shaped groove with two layers of branches, (9) inverted fir tree-shaped groove with four layers of branches, (10) spindle-shaped groove, (11) double spindle-shaped groove, and (12) quadruple spindle-shaped groove); and the combined category ((13) fir tree-shaped groove with one layer of branches, (14) fir tree-shaped groove with two layers of branches, (15) fir tree-shaped groove with four layers of branches, (16) angle-opened Lello triangular groove, and (17) edge-opened Lello triangular groove).

The consistency of the parameters is a prerequisite for structural optimisation. However, some particular cases arise when using uniform geometric parameters. For example, the expansion angle and radial width of a circular groove are both related to the diameter of the circle. Moreover, the expansion angle of a semicircular groove or semicircular ring groove equals the radius, while the radial width equals the diameter. The same situation occurs with Lello triangles, where simultaneously satisfying the requirements of the expansion angle and radial width specified in Table 1 for geometric parameters is complex. Therefore, when comparing all groove types, this study considered the root diameter and the number of grooves as the primary parameters, while the expansion angle was considered a secondary parameter. This approach ensures the consistency of all groove types regarding the groove–dam ratio and number of grooves. The groove–land ratio remained consistent in most cases except for the few particular cases mentioned above. For those cases, the groove–land ratio varied. Therefore, the strategy adopted in this study was to set the groove–land ratio, which was consistent in most cases, to the midpoint between the high and low values. This configuration compensates for the differences in individual particular cases and enhances the persuasiveness of the subsequent performance analysis of these 17 groove types. Such meticulous parameter settings can provide strong evidence to support structural optimisation in subsequent analyses.

First, each groove type was evaluated based on the proportion of the high-pressure area each type generated. This study focused on the colour distribution of the pressure cloud map for each groove type, particularly the size and continuity of the red and orange areas, representing higher pressure. The widespread distribution of high-pressure areas indicates the potential of the groove type in forming dynamic pressure effects and high-pressure barriers. The rectangular groove (1) exhibited the largest proportion of high-pressure areas,

followed by the circular and Lello triangular grooves (4, 16, 17), and quadruple grooves with sharp angles (9, 12, 15) also had relatively large high-pressure areas. The inverted T-shaped groove (3) and the fir tree-shaped groove with two layers of branches (14) exhibited relatively smaller proportions of high-pressure areas. Subsequently, each groove type was evaluated based on the peak pressure each type generated. The spindle-shaped groove (10) had the highest peak pressure, likely related to its two oblique edges effectively guiding the flow inside the groove to a sharp point. The semicircular ring groove (6) and inverted T-shaped groove (3) had smaller peak values.

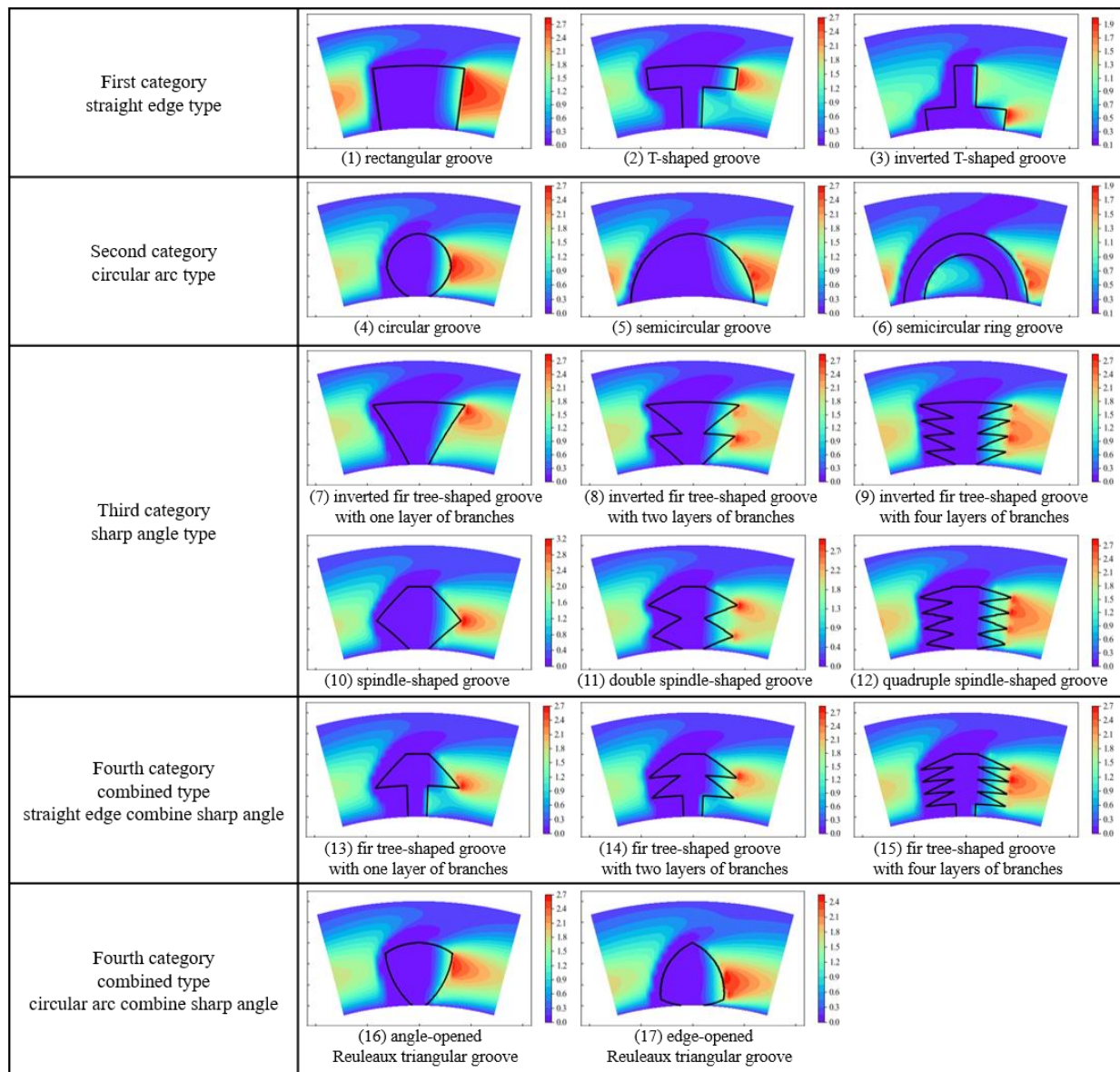


Figure 7. Pressure distribution of 17 types of bi-directional rotating grooves.

3.2.3. Sealing Performance Parameters

The performance of the groove types was evaluated based on the principle of balancing the opening force with the closing force. Uniform geometric parameters and operating conditions were set (see Tables 1 and 2), with a rotational speed of 20,000 r/min, a pressure of 101.325 kPa on the high-pressure side, a temperature of 100 °C, and an oil–air ratio of 0.03. The groove types automatically adjust their average film thickness to generate an opening force that can balance the closing force. The adjustment differs according to the

groove type. Therefore, among groove types with the same opening force, the one that produces lower leakage rates was considered to provide better pumping efficiency and, thus, was deemed optimal at that point.

Herein, the seal chamber is defined as the inlet and the surroundings are defined as the outlet. The positive/negative sign of the leakage rate indicates the flow direction. A positive leakage rate indicates leakage from the inlet to the outlet, i.e., the oil–air fluid leaking from the seal chamber to the outside. A negative leakage rate indicates leakage from the outlet to the inlet or from the surrounding to the seal chamber. The negative leakage rate represents the pumping rate.

Figure 8 shows that the pumping effect of inverted fir tree-shaped grooves is generally good, while rectangular grooves are slightly inferior. Among them, the inverted fir tree-shaped groove with one layer of branches (7) has the best pumping effect. The pumping effect of inverted T-shaped grooves (3), semicircular grooves (5), and semicircular ring grooves (6) is relatively weak. The pumping effect of the inverted fir tree-shaped groove with one layer of branches (7) is even 633.54% that of the semicircular ring grooves (6). If the rotational speed is gradually reduced, the groove type that may first experience leakage could be the semicircular ring groove.

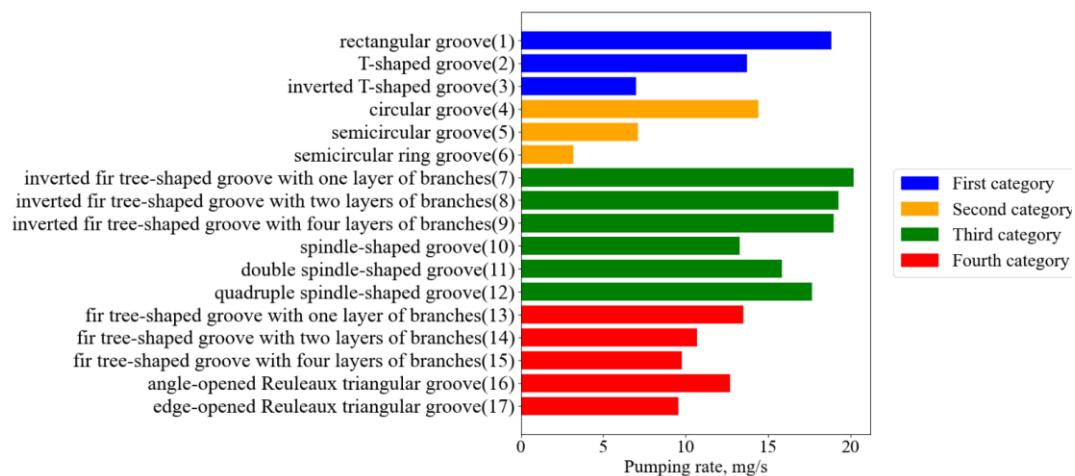


Figure 8. Comparison of pumping rates for the 17 groove types under force balance.

In comparison, while the pressure distribution and peak pressure are important and indeed have great potential in forming dynamic pressure effects and high-pressure barriers, excessively high dynamic pressure effects can lead to large sealing clearances, which widen the leakage channels and ultimately reduce the overall pumping efficiency.

3.3. Effects of Operating Parameters on the Performance of Micro-Grooved Pumping Seal

The inverted fir tree-shaped groove with one layer of branches (7) is the optimal among the 17 groove types. This section analyses the effects of rotational speed, oil–air ratio, inlet pressure, and temperature on the sealing performance of this groove type separately. For a straightforward analysis, the variations in operating parameters in this section were conducted under conditions of fixed film thickness.

3.3.1. Effects of Rotational Velocity on Performance of Micro-Grooved Pumping Seal

Figure 9 shows the computed opening forces and leakage rates at different rotational velocities ranging from 2000 to 80,000 r/min, with other parameters set to the values listed in Tables 1 and 2.

As shown in Figure 9, the opening force increases nonlinearly with the rotational velocity, indicating that a higher rotational velocity leads to a stronger hydrodynamic effect on the inverted fir tree-shaped groove with one layer of branches (7) and, thus, a higher opening force. The pumping rate first increased nonlinearly, decreased with rotational

velocity, and then gradually stabilised. This variation trend in the pumping rate indicates that for a particular setting of other operating and structural parameters of the sealing ring, an optimal operating point for rotational velocity exists, where the pumping rate peaks at around 28,000 rpm. Additionally, a limit to the pumping rate at extreme rotational speeds is present, where the pumping rate stabilises after exceeding 50,000 rpm. This is because, as the rotational speed increases, the radial velocity of the medium also increases, thereby enhancing the pumping effect. However, as the hydrodynamic effect becomes stronger, the stiff air film in the dam area blocks the pumping path, causing the pumping rate to decrease to some extent. Ultimately, the hydrodynamic effect and the pumping effect balance each other out. Therefore, after the speed reaches 50,000 rpm, simply increasing the rotational speed will not improve the sealing effect.

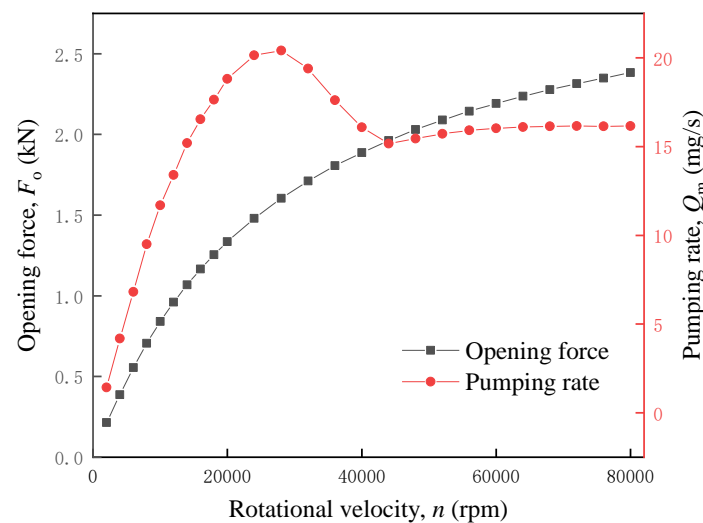


Figure 9. Opening forces and leakage rates at different rotational velocities.

3.3.2. Effects of Oil–Air Ratio on Performance of Micro-Grooved Pumping Seal

Figure 10 shows the computed opening forces and leakage rates at different oil–air ratios ranging from 0.01 to 0.1, with other parameters set to the values listed in Tables 1 and 2.

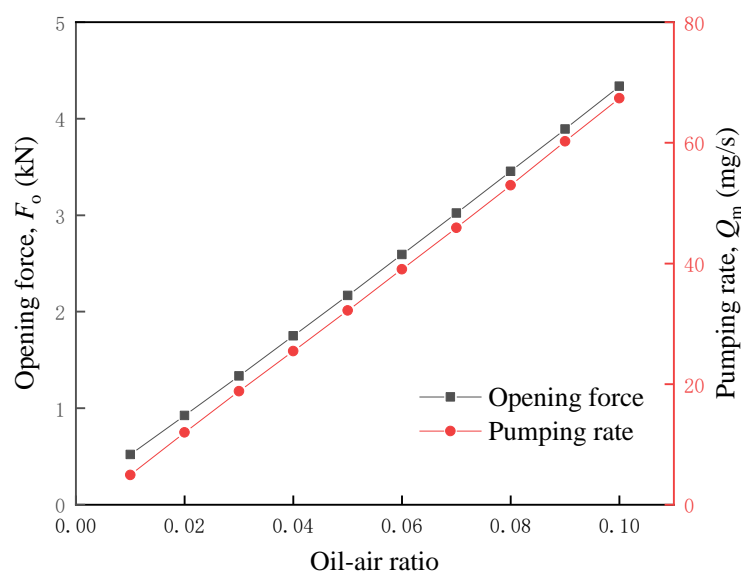


Figure 10. Opening forces and leakage rates at different oil–air ratios.

As shown in Figure 10, the opening force increases approximately linearly with the oil–air ratio. This result can be explained by the following mechanism: as the oil–air ratio increases, the equivalent density and viscosity of the oil–air two-phase fluid increases, increasing the bearing capacity and opening force. Similarly, the pumping rate increases approximately linearly with the oil–air ratio. As indicated in Equation (10), an increase in the equivalent density inevitably increases the pumping rate when computing the leakage mass rate.

3.3.3. Effects of Inlet Pressure on the Performance of Micro-Grooved Pumping Seal

Figure 11 shows the computed opening forces and leakage rates at different inlet pressures ranging from 0 to 300 kPa, with other parameters set to the values listed in Tables 1 and 2.

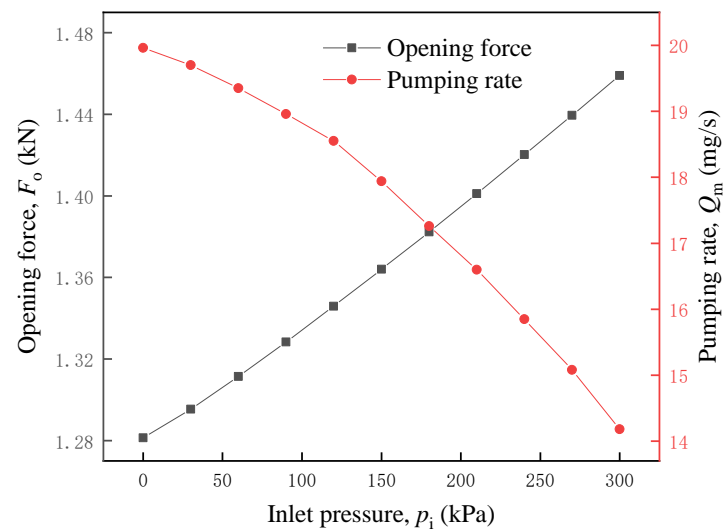


Figure 11. Opening forces and leakage rates at different inlet pressures.

As shown in Figure 11, the opening force increases approximately linearly with the inlet pressure. This result can be explained by the following mechanism: an increase in the inlet pressure increases the equivalent density and viscosity of the oil–air two-phase fluid between the end faces, thereby increasing the bearing capacity. The opening force equals the pressure integration within the entire flow field. This explains why the opening force of the gas film increases as the inlet pressure increases. Additionally, the pumping rate decreases nonlinearly with the inlet pressure. This is because increasing the inlet pressure increases the difference between the pressures at the inner and outer radii of the sealing ring, increasing the flow of the two-phase fluid from the seal to the surroundings. When the pumping effect of the inverted fir tree-shaped groove with one layer of branches (7) is insufficient to counteract the pressure difference-induced outflow, the pumping rate inevitably decreases and changes to positive. Moreover, the leakage rate increases with the inlet pressure.

3.3.4. Effects of Temperature on the Performance of Micro-Grooved Pumping Seal

Figure 12 shows the computed opening forces and leakage rates at different temperatures ranging from 60 to 110 °C, with other parameters set to the values listed in Tables 1 and 2.

As shown in Figure 12, the opening force decreases as the temperature increases. The temperature mainly affects the equivalent viscosity of the oil–air two-phase fluid. As temperature increases, air viscosity increases, and the lubricant viscosity decreases. While the oil–air ratio is small, the viscosity of the lubricant is significantly higher than that of air. Therefore, the equivalent viscosity mainly depends on the lubricant viscosity.

This explains why the equivalent viscosity of the oil–air fluid decreases as the temperature increases. Additionally, a decrease in the equivalent viscosity decreases the viscous shear force and, consequently, the hydrodynamic effect. This explains why an increase in temperature decreases the opening force. The pumping rate increases nonlinearly with an increasing temperature due to the temperature-induced variations in the equivalent viscosity. A decrease in the equivalent viscosity of the oil–air fluid increases its fluidity and, consequently, the pumping rate. Additionally, as expressed in Equation (6), the viscosity of the lubricant varies exponentially with temperature. In contrast, as shown in Figure 12, the pumping rate varies exponentially with the temperature, exhibiting a significant exponential increase when the temperature exceeds 80 °C. This phenomenon can be referred to as a temperature-induced abrupt increase in pumping rate.

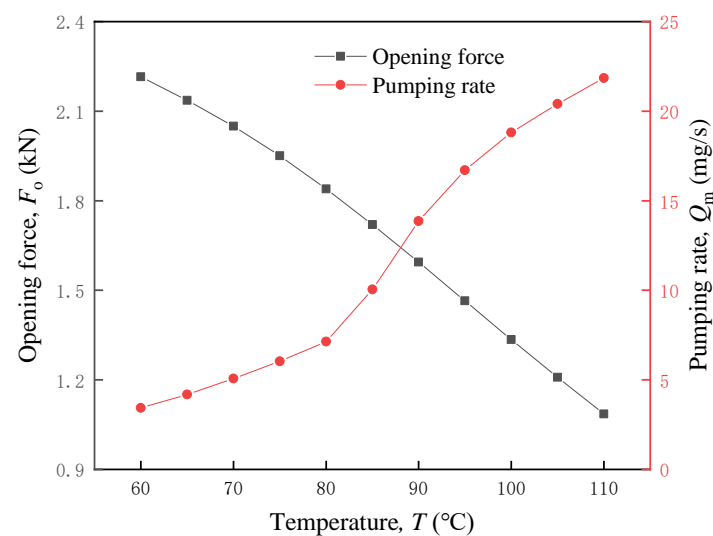


Figure 12. Opening forces and leakage rates at different temperatures.

4. Conclusions

This study investigated 17 micro-grooved pumping seals for EVs, with the real gas effect and viscosity described using the virial and Lucas equations, respectively, and using the oil–air ratio to determine the equivalent density and viscosity of the two-phase fluid formed with the mixture of the lubricant and air in the seal. The compressible steady-state Reynolds equation was solved using the finite difference method. The pumping mechanisms of the seal and the effects of its operating parameters (rotational velocity, oil–air ratio, inlet pressure, and temperature) on the steady-state sealing performance were analysed.

This study's findings indicate that the high-speed micro-grooved pumping seal for new energy vehicles induces a significant hydrodynamic effect when the lubricant and air mixture form a two-phase fluid, affecting the pumping rate across the entire sealing face. The optimal design, identified as the inverted fir tree-shaped groove with one layer of branches, performs best under typical operating and geometric parameters. The opening force of this seal increases with rotational velocity, oil–air ratio, and inlet pressure but decreases with temperature, with the oil–air ratio having the most significant effect. Additionally, the pumping rate exhibits a non-linear behaviour with rotational velocity, first increasing and then decreasing, but increasing with oil–air ratio and temperature while decreasing with inlet pressure. Critical factors for seal design include the optimal operating point for rotational velocity, the limit to the pumping rate at extreme speeds, and the temperature-induced abrupt increase in pumping rate.

Based on the findings of this study, future research can focus on the impact of seal materials and groove geometries on sealing performance, the steady-state performance under the coupling of fluid–structure–thermal interactions, and the dynamic performance

of gas–liquid two-phase dynamic pressure seals. This will contribute to a better understanding of the behaviour of seals in practical applications, further improving their sealing effectiveness under high-speed and unstable conditions and providing more reliable sealing solutions for new energy vehicles.

Author Contributions: Conceptualisation: H.C., X.D. and R.Y.; methodology: H.C., X.D. and R.Y.; software: H.C. and R.Y.; validation: H.C.; formal analysis: H.C.; investigation: X.H. and X.B.; resources: X.D., R.Y., X.H. and X.B.; data curation: H.C.; writing—original draft preparation: H.C.; writing—review and editing: H.C.; visualisation: H.C.; supervision: X.D. and R.Y.; project administration: H.C., X.D. and R.Y.; funding acquisition: X.D. All authors have read and agreed to the published version of the manuscript.

Funding: This work was supported by the National Key Research and Development Program of China, grant number 2020YFB2010001.

Data Availability Statement: Data are contained within this article.

Acknowledgments: The authors are grateful to the anonymous reviewers for their careful and detailed comments.

Conflicts of Interest: Authors Xianzhi Hong and Xin Bao were employed by Chengdu Yitong Seal Co., Ltd. The remaining authors declare that the research was conducted in the absence of any commercial or financial relationships that could be construed as a potential conflict of interest. Chengdu Yitong Seal Co., Ltd. had no role in the design of the study; in the collection, analyses, or interpretation of data; in the writing of the manuscript; or in the decision to publish the results.

References

- Ran, D.C. Analysis on the development of the automobile industry under the carbon peaking and carbon neutrality goals. *Mark. Wkly.* **2023**, *36*, 49–52.
- Shang, K. The Global New Energy Vehicle Industry Is Accelerating Its Development. *People's Daily*, 1 December 2022.
- Yang, Z. Electric Drive System Technology Has Become a Competitive Hotspot. *China Energy News*, 15 August 2022.
- Liu, C.Z.; Zhang, T.; Song, J.; Yin, X.; Ge, S. Study on coupling dynamics of electric drive system of pure electric vehicle. *Automot. Eng.* **2022**, *44*, 1896–1909.
- Liang, X.L. Development and application of new energy vehicle gearbox PTFE oil seal. *Intern. Comb. Eng. Parts* **2019**, *7*, 27–28.
- Grün, J.; Feldmeth, S.; Bauer, F. Wear on radial lip seals: A numerical study of the influence on the sealing mechanism. *Wear* **2021**, *476*, 203674. [[CrossRef](#)]
- Chen, L.; Lin, W.; Han, Y.W.; Ai, Z.J.; Kuang, Y.C.; Yang, C.L. Simulation and experimental study of a new structural rubber seal for the roller-cone bit under high temperature. *Adv. Mech. Eng.* **2020**, *12*, 1–13. [[CrossRef](#)]
- Choi, H.J.; Park, C.W.; Lee, J.C.; Kim, J.G.; Choi, S.D. Analysis on the mechanical characteristics of PTFE oil seal for the rear part in the automotive engine. *Int. J. Precis. Eng. Manuf.* **2011**, *12*, 485–490. [[CrossRef](#)]
- Huang, T.C.; Lin, C.Y.; Liao, K.C. Sealing performance assessments of PTFE rotary lip seals based on the elasto-hydrodynamic analysis with the modified archard wear model. *Tribol. Int.* **2022**, *176*, 107917. [[CrossRef](#)]
- Mei, B.F.; Hu, B. Development and experimental research of a new type of low friction engine oil seal. *China Auto.* **2022**, *5*, 44–48.
- Nino, D. Elastohydrodynamic lubrication analysis of a radial oil seal with hydrodynamic features. *Tribol. Int.* **2022**, *173*, 107653.
- Jiang, H.S. The hydrodynamic oil seals research current situation and prospects. *Hydraul. Pneumol. Seal.* **2018**, *38*, 1–5.
- Tan, S.L. *Sealing Performance of Automotive Steering Gear Oil Seal Material and the Study of Friction and Wear*; Lanzhou Jiaotong University: Lanzhou, China, 2023.
- Jiang, Y.J. *Preparation and Properties of PTFE Composites for Rotary Shaft Oil Seal Lip Sheet Application*; Xihua University: Chengdu, China, 2023.
- Xie, J. *Theoretical and Experimental Study on Thermo-Hydrodynamic Lubrication of Elliptical Groove Gas Face Seals*; Zhejiang University of Technology: Zhejiang, China, 2020.
- Xudong, P.; Yuelin, Z.; Shaoxian, B.A.I.; Jiyun, L.I.; Song'en, S. Effect of rotational speed and sealing medium pressure on optimization of groove geometric parameters of a T-groove dry gas face seal. *CIESC J.* **2012**, *63*, 551–559.
- Su, H.; Rahmani, R.; Rahnejat, H. Performance evaluation of bidirectional dry gas seals with special groove geometry. *Tribol. Trans.* **2017**, *60*, 58–69. [[CrossRef](#)]
- Shahin, I. Gas seal performance and start up condition enhancing with different seal groove geometries. *J. Aeronaut. Aerosp. Eng.* **2016**, *5*, 1–9.
- Yang, X.Q.; Wang, Y.F.; Ma, G.F. Numerical analysis of the steady-state characteristics of v-groove opening angle on end face dry gas seals. *Auto. Appl. Technol.* **2023**, *48*, 60–66.

20. Wang, Y.; Sun, J.J.; Tao, K.; Chen-bo, M.A.; Qiao-an, T.U. Numerical analysis of t-groove dry gas seal and groove optimization. *Tribology* **2014**, *34*, 420–427.
21. Yan, W.; Jianjun, S.; Chenbo, M. Research progress in the bi-direction noncontact mechanical seal technology. *Fluid Mach.* **2013**, *41*, 34–40.
22. Yu, M.B.; Meng, X.K.; Bai, S.X. Analysis of a hydrodynamic face seal with circular grooves on to its surface. *Lubr. Eng.* **2009**, *34*, 33–35.
23. Yan, R.Q.; Wang, R.X.; Xu, J.; Ding, J.H.; Chen, H.Q.; Wang, S.P.; Ding, X.X.; Zhang, W.Z. The Utility Model Relates to a Lello Triangle Groove Sealing Ring Suitable for Three-Phase Sealing. CN213628878U [P/OL]. Available online: <https://pta.cnki.net/patent/PatentSearch/PatentSearchResult.aspx> (accessed on 15 May 2024).
24. Poling, B.E.; Prausnitz, J.M.; O'connell, J.P. *The Properties of Gases and Liquids*; McGraw-Hill: New York, NY, USA, 2001.
25. Li, S.C.; Qian, C.F.; Li, S.X.; Chen, L. Study of thermal-fluid-solid coupling on dynamic characteristics of oil-gas miscible backflow pumping seal. *CIESC J.* **2020**, *71*, 2190–2201.
26. Li, S.; Qian, C.; Li, S.; Zhong, J.; Liu, X. Face micro-deformation and its control method of rotating ring of hydrodynamic face seal under high speed, high pressure and wide temperature range. *J. Beijing Univ. Aeronaut. Astronaut.* **2021**, *47*, 1173–1185.
27. Li, S.C.; Qian, C.F.; Li, S.X.; Li, Q.; Liao, H. Study of sealing mechanism of gas-liquid miscible backflow pumping seal. *Tribol. Int.* **2020**, *142*, 105974. [[CrossRef](#)]
28. Li, Q.Z. *Research on Starting Performance of Gas-Liquid Miscible Reflux Pumping Seal*; Beijing University of Chemical Technology: Beijing, China, 2020.
29. Li, Q.Z.; Li, S.X.; Zheng, R.; Li, N.; Li, S.C. Opening temperature characteristics of reflux pumping seal based on optimum parameters. *Aeroengine* **2021**, *47*, 72–79.
30. Li, Q.Z.; Li, S.X.; Zheng, R.; Chen, L.; Li, S. Test analysis on the opening process of oil-gas miscible reflux pumping seal. *Aeroengine* **2020**, *46*, 22–27.
31. Li, Q.Z.; Zheng, R.; Li, S. Comparative analysis and experiment on gas-phase and liquid-phase performance of high-speed hydrodynamic seal. *J. Harbin Inst. Technol.* **2019**, *51*, 70–75.
32. Li, Q.Z.; Zheng, R.; Li, S.X.; Chen, L.; Li, S.C. Follows dynamic characteristics of oil-gas two-phase hydrodynamic seals based on fluid-solid-thermal coupling. *J. Harbin Inst. Technol.* **2020**, *52*, 122–132.
33. Chen, L.; Li, S.X.; Li, H.; Li, S.C.; Li, Q.Z. Analysis and experiment verification on end-face temperature distribution of oil-gas two-phase backflow pumping seal. *Lubr. Eng.* **2019**, *44*, 122–128.
34. Li, H. *Performance Study of Oil-Gas Two-Phase Backflow Pumping Seal*; Beijing University of Chemical Technology: Beijing, China, 2017.
35. Li, H.; Li, S.X.; Li, X.F.; Cai, J.N.; Zhang, Q.X.; Wang, L. Multi-parameter optimization and orthogonal experimental study of a two-phase oil and gas dynamic pressure seal structure. *J. Beijing Univ. Chem. Technol. (Nat. Sci. Ed.)* **2017**, *44*, 76–84.
36. Yan, R.; Chen, H.; Zhang, W.; Hong, X.; Bao, X.; Ding, X. Calculation and verification of flow field in supercritical carbon dioxide dry gas seal based on turbulent adiabatic flow model. *Tribol. Int.* **2022**, *165*, 107275. [[CrossRef](#)]
37. Wen, S.Z.; Huang, P.; Tian, Y.; Ma, L.R. *Principles of Tribology*, 5th ed.; Tsinghua University Press: Beijing, China, 2018.

Disclaimer/Publisher's Note: The statements, opinions and data contained in all publications are solely those of the individual author(s) and contributor(s) and not of MDPI and/or the editor(s). MDPI and/or the editor(s) disclaim responsibility for any injury to people or property resulting from any ideas, methods, instructions or products referred to in the content.